IOP Publishing Journal of Physics: Condensed Matter

J. Phys.: Condens. Matter **27** (2015) 133203 (15pp) doi:10.1088/0953-8984/27/13/133203

Topical Review

Interfacing graphene and related 2D materials with the 3D world

David Tománek

Physics and Astronomy Department, Michigan State University, East Lansing, MI 48824, USA

E-mail: tomanek@pa.msu.edu

Received 1 January 2015, revised 3 February 2015
Accepted for publication 5 February 2015
Published 17 March 2015

Abstract

An important prerequisite to translating the exceptional intrinsic performance of 2D materials such as graphene and transition metal dichalcogenides into useful devices precludes their successful integration within the current 3D technology. This review provides theoretical insight into nontrivial issues arising from interfacing 2D materials with 3D systems including epitaxy and ways to accommodate lattice mismatch, the key role of contact resistance and the effect of defects in electrical and thermal transport.

Keywords: graphene, phosphorene, interface, Schottky barrier, 2D semiconductor, transition metal dichalcogenides

(Some figures may appear in colour only in the online journal)

1. Interest in 2D structures

Current high level of interest in graphene and related 2D materials is primarily linked to their exceptional intrinsic electrical and thermal transport properties [1]. The unusually long electron and phonon mean free path found in graphene [2], which plays a key role in its excellent charge and heat transport behavior, has previously been observed in structurally related carbon nanotubes and has motivated research in these 1D systems during the preceding two decades. Since a 1D nanotube may be formed by rolling up and seamlessly connecting the edges of a 2D layer, graphene and nanotubes display very similar behavior. Lessons learned from nanotubes of whichever material will be applicable to their planar counterparts and vice versa. Among the problems that have hindered a successful deployment of carbon nanotubes in high-end electronic devices, the difficulty to form a well-defined interface between these 1D systems and the 3D world reproducibly has been one of the most challenging. The same limitation applies to 2D systems and needs to be addressed with the same care.

A large number of elements and compounds in nature form layered structures. Besides the most popular graphite, other compounds of interest include hexagonal BN (h-BN), transition metal dichalcogenides (TMDs) including MoS_2, black phosphorus and grey arsenic, BC_3 and vanadium oxide. The weak inter-layer interaction with a dominant van der Waals component allows mechanical cleavage to form monolayers or few-layer systems. Among these, probably the best studied is graphene, followed by h-BN, TMDs, and more recently by phosphorene. For many of these systems, chemical vapor deposition (CVD) has emerged as a viable synthesis approach that is more scalable than mechanical exfoliation. It is an open question whether also molecular beam epitaxy (MBE) will become a viable contender to CVD to grow 2D monolayers.

As thin films, all of these systems share some unique electronic and mechanical properties. If it were not for its vanishing fundamental band gap, graphene would probably be without competition in terms of mechanical, thermal and chemical stability, excellent charge and heat transport, and mechanical flexibility. Other monolayer systems mentioned above share a nonzero intrinsic band gap, an important prerequisite for semiconductor applications, but typically do not measure up to graphene in at least one of its other beneficial properties.

It is common knowledge that heat production in high-speed electronics requires active thermal management that is currently approaching its limits. Therefore, thermal conductivity and formation of good thermal contacts play

as important a role in 2D materials as charge transport. Whereas graphene is a semi-metal and thus not suitable for semiconducting applications, it has a very high carrier mobility, which intrinsically semiconducting MoS_2 and phosphorene monolayers can not match. Multiple approaches have been proposed to open up a band gap in graphene, including formation of finite-width graphene nanoribbons and chemical functionalization, but the modified structures do not offer reproducible performance and display lower charge and thermal conductance than their pristine counterparts. Other modifications causing a change in the electronic structure near the Fermi level in layered systems include strain and changing the number of layers [3–6].

2. Challenges posed by interfacing 2D structures with the 3D world

The first challenge to scientists is to *fabricate defect-free 2D films* that may subsequently be transferred onto a 3D substrate, forming an optimum interface. What has become the most popular way to form and characterize monolayers of graphene involves mechanical cleavage of graphite using a Scotch tape [7], followed by transfer onto a substrate. This technique has been subsequently applied to other layered substances such as MoS_2 [8] and other transition metal dichalcogenides (TMDs), as well as black phosphorus [3, 9].

Mechanical cleavage produces rather perfect monolayers, but is not scalable and thus of little interest for future large-scale applications. Chemical exfoliation, pioneered half a century ago [10], leaves chemical residue behind. More recently, CVD has emerged as a viable alternative capable of producing large monolayers on suitable substrates. While especially notable progress has been achieved in the formation of graphene monolayers on transition metal substrates [11–14], CVD has also been applied to form monolayers of other systems including hexagonal boron nitride [15]. The main drawback of using CVD is a higher concentration of structural defects. Even under optimized synthesis conditions, it is apparently impossible to avoid the simultaneous growth of grains, which typically inter-connect by non-hexagonal rings at the grain boundary, forming line defects [16]. Grain boundaries are linked not only to growth kinetics in CVD, but become also a means to accommodate lattice mismatch and to reduce strain at the interface between a 2D structure and an incommensurate substrate.

The properties of a 2D structure interfaced with a 3D structure are not merely dictated by the quality of the components. A significant challenge is to *provide an optimum interface* between the 2D and 3D structure. The efficiency of charge carrier injection depends sensitively on several parameters characterizing the interface that will be discussed in section 4. Since charge transport is always accompanied with heat evolution, thermal management plays an ever increasing role especially in nanostructured electronic devices. The ability to use a 3D structure as a heat sink for a 2D layer precludes a good thermal contact between the two structures, which in turn also depends on the microscopic structure at the interface.

3. Equilibrium structure of ultrathin films

It may appear surprising that a wide range of systems with a cubic structure in the bulk should transform spontaneously to layered graphitic structures in ultrathin films [17]. This unusual claim is supported by total energy calculations, which show that the layered graphitic structure is often the most stable atomic arrangement in ultrathin films of systems ranging from carbon and boron nitride to silicon carbide, boron phosphide and even rocksalt [17]. The reason for this finding is the dominant role of the surface region in ultrathin films.

For the sake of a simple argument, let us subdivide the structure of an N-layer slab into the surface region containing 2 (bottom and top) layers and the bulk region containing $N-2$ layers. Let us distinguish between two types of sites, namely sites with bulk-like environment and binding energy $E(\text{bulk})$ and surface sites with missing neighbors and binding energy $E(\text{surface})$. The total binding energy of the slab is then

$$E(N\text{-layer slab}) = 2E(\text{surface}) + (N-2)E(\text{bulk})\,. \quad (1)$$

Let us furthermore consider the energy competition between two structures, namely the bulk (cubic) structure and a graphitic layered structure. To do so, we define the energy difference

$$\Delta E = E_{\text{gra}} - E_{\text{cub}} \quad (2)$$

for either the bulk or the surface region. The sign of $\Delta E(\text{slab})$, given by

$$\Delta E(N\text{-layer slab}) = 2\Delta E(\text{surface}) + (N-2)\Delta E(\text{bulk}) \quad (3)$$

decides, whether the preferential atomic arrangement in a slab resembles more the bulk (cubic) structure or the layered graphitic structure. The answer is clear in very thick slabs with $N \to \infty$, which have the bulk (cubic) structure due to the negligible role of the surface. In ultrathin slabs, however, should the sign of $\Delta E(\text{surface})$ differ from that of $\Delta E(\text{bulk})$, the energetic preference for the graphitic structure at the surface may drive a structural transformation to a graphitic structure in ultrathin slabs with a dominant role of the surface.

Graphitization tendency at surfaces is rather common, since the surface energy of layered honeycomb structures is commonly lower than that of their cubic counterparts with close-packed (1 1 1) surfaces. Even though the physical origin may be different, the surface energy reduction upon conversion from a bulk (cubic) to a graphitic structure is common to systems with purely covalent or purely ionic bonding, or a combination of the two. The competing cubic and layered graphitic phases of carbon with a bulk diamond lattice, boron phosphide with a bulk zincblende lattice, and NaCl with a bulk rocksalt lattice are illustrated in figure 1(*a*).

Reduction of the surface energy at bare surfaces is believed to cause graphitization of diamond nanoparticles [18] and nanowires [19], as well as ultrathin diamond [20], SiC [21] and ZnO [22] films. This simple consideration may turn into a valuable bottom-up approach to synthesize hypothetical ultrathin layered structures [23] for nanoelectronics applications in the post-graphene era.

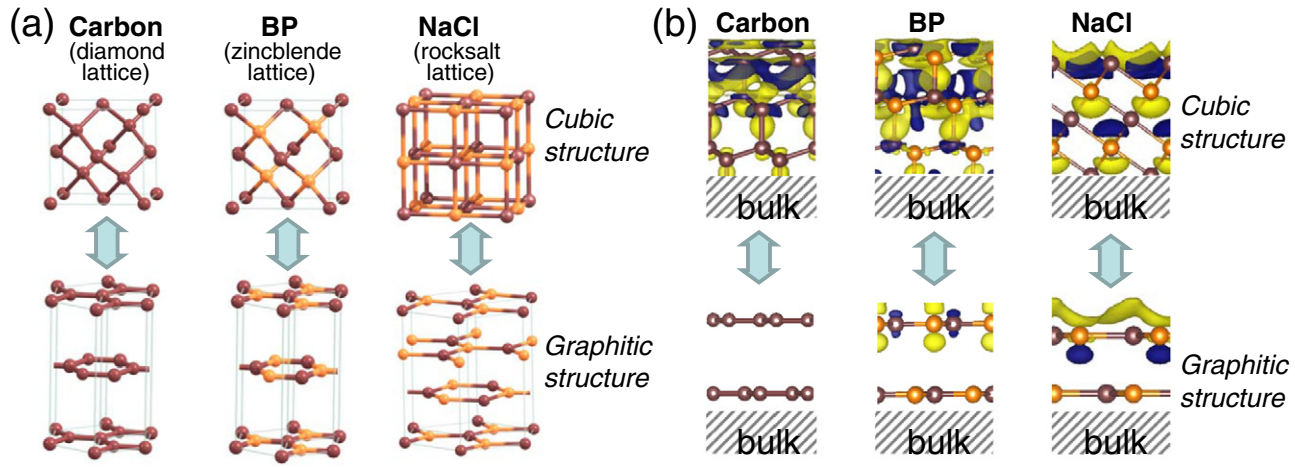

Figure 1. (*a*) Ball-and-stick models of diamond, zincblende, and rocksalt in their native bulk structure (top panels) and their corresponding layered counterparts (bottom panels). (*b*) Total charge density difference $\Delta\rho$ between the slab and the bulk structure near the (1 1 1) surface of carbon, BP and NaCl in the bulk cubic (top panels) and the layered graphitic (bottom panels) phase, superposed with the atomic structure. The isosurface values $\Delta\rho_{\pm} = \pm 5\times10^{-4}$ e Å^{-3} allow to distinguish between regions with electron excess, shown by the dark (blue) isosurfaces, and regions with electron deficit, indicated by the light (yellow) isosurfaces. Adapted from [17], © 2014 American Chemical Society.

The surface energy, corresponding to half the energy required to cleave a crystal, represents the binding energy difference between bulk and surface atoms. In cubic crystals, cleavage is typically associated with a large charge redistribution in the surface region due to the significantly changed atomic environment. This can be visualized by the charge density difference $\Delta\rho = \rho(\text{slab}) - \rho(\text{bulk})$ that is displayed in the top panels of figure 1(*b*) for carbon, BP and NaCl. The extent of charge redistribution in the surface region correlates well with the surface energy. The charge redistribution caused by cleaving layered graphitic structures of these systems, shown in the bottom panels of figure 1(*b*) is much smaller than in the cubic counterparts. Also the surface energy of the graphitic structures is lower, since cleavage does not change significantly the atomic environment.

Using binding energy values listed in [17], it is possible to determine the dependence of the slab cohesive energy difference $\Delta E(N\text{-layer slab})$ on the number of layers N using equation (3). Results for (1 1 1) terminated ultrathin films of C, BN, Si, SiC, BP and NaCl are presented in figure 2. For $N \to \infty$, these results are consistent with the energetic preference of bulk Si, SiC, BP and NaCl for the cubic structure, and that of C and BN for the layered graphitic structure. The critical slab thickness N_c, below which a graphitic slab structure is most stable, is indicated by $\Delta E(N\text{-layer slab}) = 0$. Our most intriguing result is that $N_c > 1$ in many systems with a well-established cubic structure in the bulk, indicating their spontaneous graphitization tendency in ultrathin films.

These results also indicate no graphitization tendency in ultrathin NaCl films terminated with a (0 0 1) surface and in silicon films. Observation of thin films of silicon deposited on a substrate is not an indication for the stability of free-standing silicene, since the films are stabilized by strong adhesion to a substrate. The non-planar, buckled structure of these films indicates their instability and energetic preference for a 3D bulk environment [24–28].

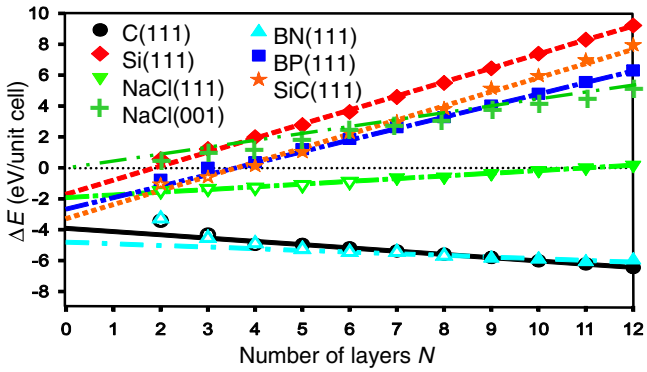

Figure 2. Binding energy difference ΔE of N-layer slabs with cubic and graphitic structure, with $\Delta E < 0$ indicating energetic preference for graphitization. Data points are results of DFT calculations. Solid symbols represent structures with locally stable cubic and graphitic phase. Open symbols represent structures with an unstable cubic phase. Lines represent predictions based on equation (3). Adapted from [17], © 2014 American Chemical Society.

As already indicated in the example of silicon films, structural changes in ultrathin slabs may also be modified deliberately by changing the binding energy of surface atoms $E(\text{surface})$ by chemisorption of atoms, molecules, or by bringing the surface into contact with a substrate. Such changes include a postulated conversion of thin films of layered hexagonal BN to a cubic phase upon fluorination [29] or the conversion of few-layer graphene to diamond upon fluorination or hydrogenation [30]. Energetic preference for a particular structure may be enhanced by a judicious choice of the substrate [23, 31].

4. Electrical contacts to 2D structures

Many 2D structures display a very long electron mean free path. The most prominent example is graphene with an

electron mean free path $\lambda_{mfp} \lesssim 1\,\mu$m at room temperature [2]. Intrinsic transport is ballistic for device sizes below λ_{mfp} and limited by emission of optical phonons otherwise. In most cases of interest, 2D structures of interest are connected to other, typically 3D structures to form a useful device. Transport in such devices is usually limited not by the intrinsic properties of the 2D structure, but more severely by the contacts. Unlike in macro-structures, understanding carrier injection through a contact to a 2D nanostructure requires quantum mechanical treatment. Since contacts limit transport, they should be treated seriously as quantum devices.

Contrary to popular perception, contacts often play a more crucial role in nanoscale electronics than the semiconducting material itself [32, 33]. Whereas contacts in Si-based submicron devices are no longer considered a problem after many decades of optimization, engineering optimum contacts to electronic nano-devices consisting of silicon [34] or carbon (e.g. nanotubes or graphene) [32, 35] has become a major challenge in the field.

4.1. Contacts as quantum devices

In the quantum mechanical description, an electrical contact is called transparent, when an incoming charge carrier has a high probability to be transmitted. This transmission probability T depends on the electronic density of states on both sides of the contact, the shape and the height of the tunnel or Schottky barrier. T is reduced in the case of Fermi velocity mismatch between the two materials brought into contact. The size of the contact region, atomic-scale registry or epitaxy at the interface, and efficient hybridization of electronic states at both sides of the interface play an important role in establishing a transparent contact. Some of these key issues will be elucidated in the following, when discussing successful strategies to optimize contacts to graphene, carbon nanotubes and transition metal dichalcogenides including MoS_2 and WSe_2.

4.2. Successful strategies to maximize contact transparency

4.2.1. Optimizing metal contacts to graphitic nanostructures. Preceding the present interest in graphene as electronic material were two decades of research effort in carbon nanotubes [36] that can be viewed as seamlessly rolled-up graphene to tubes with nanometer diameter. Since both graphene and carbon nanotubes are chemically near-identical structures formed of sp^2 bonded carbon, concerns and strategies regarding formation of ideal contacts are the same for both systems. There have been strong sample-to-sample variations in the observed performance of nanotube devices, which caused many controversies; these have eventually been traced back to variations in contacts. Weak nanotube-metal coupling, found in nanotubes deposited on metal electrodes, has been shown to cause Coulomb blockade behavior [37]. In spite of significant progress in maximizing the contact area by depositing metal on top of nanotubes [38], the transparency of such contacts was still found to depend strongly on the contact metal. Whereas low contact resistance has been reported between nanotubes and Au or Au/Cr [39, 40], using Au/Ti contacts resulted in a high contact resistence [41]. The transparency

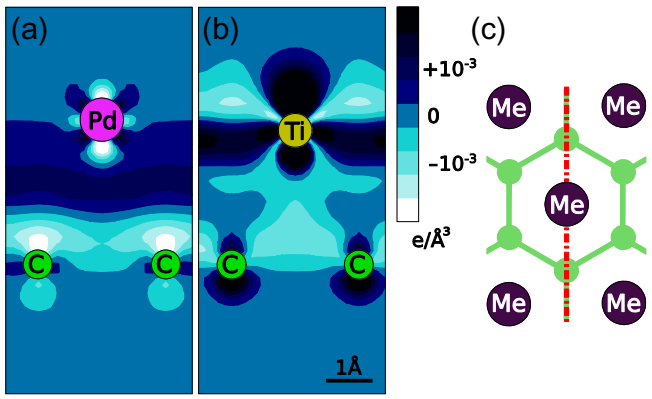

Figure 3. Charge density redistribution $\Delta\rho(\mathbf{r}) = \rho_{Me/C}(\mathbf{r}) - \rho_{Me}(\mathbf{r}) - \rho_{C}(\mathbf{r})$ in (*a*) Pd and (*b*) Ti monolayers interacting with a graphene layer, indicating regions of charge depletion and excess with respect to the superposition of isolated layers. (*c*) Schematic double-layer geometry in top view, with the cutting plane used in (*a*) and (*b*) indicated by the dash-dotted line. Reproduced with permission from [35]. Copyright 2006 by the American Physical Society.

of Pd-based contacts has been reported as superior to Ti contacts [42, 43]. This appears counter-intuitive, since Ti-C interaction is stronger than Pd-C interaction. Reports suggesting that carrier injection occurs only at the edge of the contact region [43] appear to contradict the observed dependence of the contact resistance on the length of the contact [41].

Some of the key issues explaining these observations have been elucidated in a quantum transport study of carbon nanotubes contacted by Ti and Pd electrodes [35]. The basis of this study was a density functional calculation of the electronic structure at the interface between graphene and (1 1 1) surfaces of Ti and Pd. The interatomic distances in these metals, 2.7 Å in Pd and 2.95 Å in Ti, lie close to the honeycomb spacing in graphene, 2.46 Å. This results in a favorable epitaxy that is superior to that of a gold-graphene contact. An important requirement for a good contact is a large overlap and hybridization of metal and graphene orbitals, which is reflected in the charge redistribution at the interface. The charge density change $\Delta\rho$ at the graphene-metal interface, along with the optimum geometry, is shown in figure 3. Significant charge redistribution at the interface and negligibly small charge transfer indicate covalent bonding. The fact that the covalent bonds at the Ti-C interface are stronger than those at the Pd-C interface, also indicated by larger values of $\Delta\rho$, may lead to the naïve conclusion that Ti should form superior contacts. In reality, the opposite is true.

Insight into the role of the electronic interaction at the metal-carbon interface in charge transport can be obtained by a quantum transport calculation. Results of this calculation for metal-nanotube junctions are summarized in figure 4. In the schematic view of an extended contact in figure 4(*a*), the central region of length L_0 with N_0 unit cells, describing an unperturbed nanotube, is connected at both ends to contact regions of varying length L_c with N unit cells. Net transport through this structure depends on carrier hopping along the carbon nanostructure, described by the hopping integral γ_0, and the hopping integral Δ that describes carrier hopping

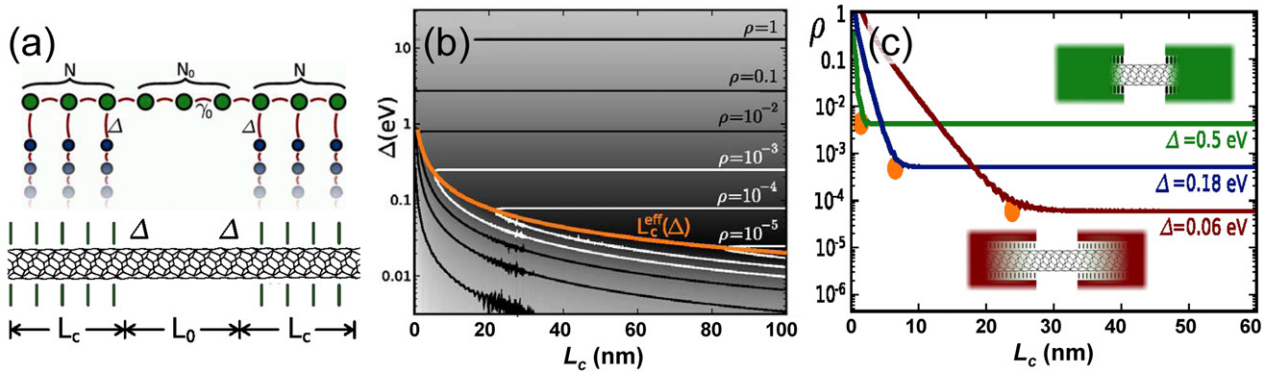

Figure 4. (*a*) Schematic geometry of a (6, 6) carbon nanotube in contact with metal leads, used in the calculation of the contact reflection coefficient ρ. (*b*) Contact reflection coefficient ρ as a function of the nanotube-metal coupling Δ and the contact length L_c. (*c*) Cuts through the contour plot (*b*) at selected values of Δ, showing ρ as a function of L_c. The effective contact length L_c^{eff} is emphasized by a heavy solid line in (*b*) and by data points in (*c*). Adapted from [35]. Copyright 2006 by the American Physical Society.

across the interface. The values of γ_0 and Δ, adjusted to reproduce the electronic structure determined by density functional calculations, are used in a tight-binding Hamiltonian that represents the electronic structure of the system.

The most significant result of a quantum transport calculation is the contact reflection coefficient ρ, which determines the contact transparency. Results of a Landauer–Büttiker quantum transport study of the metal-nanotube-metal assembly using the above described tight-binding Hamiltonian are summarized in figures 4(*b*) and (*c*). As expected, we find zero transmission corresponding to complete reflection, specified as $\rho = 1$, for a vanishing contact length, $L_c = 0$, and vanishing coupling, $\Delta = 0$. For finite values of L_c and Δ, however, it is not immediately obvious if a combination of strong coupling and short contact is superior to a combination of weak coupling and a long contact.

The contour plot in figure 4(*b*) answers this question: For any given carbon-metal coupling Δ, the contact transparency always increases with increasing contact length L_c. For any given value of L_c, however, transparency is optimized at a particular coupling Δ that is neither too small nor too large. Optimum transparency is given by (Δ, L_c) pairs that follow the valley in figure 4(*b*). The dependence of the contact reflection coefficient ρ on the contact length L_c for a particular contact metal, characterized by the value of Δ, is summarized in figure 4(*c*). For Ti with a larger value $\Delta \approx 0.3\,\text{eV}$ associated with strong Ti-C bonds, the contact reflection coefficient saturates rapidly at $\rho \approx 10^{-3}$ for $L_c \gtrsim 5\,\text{nm}$. Rather surprising is the result for Pd with a smaller value $\Delta \approx 0.06\,\text{eV}$ associated with weaker Pd-C bonds, where the contact reflection coefficient decreases more slowly and saturates only at $L_c \gtrsim 25\,\text{nm}$, but reaches a much lower value $\rho \lesssim 10^{-4}$, corresponding to a tenfold increase in contact transparency.

The net conclusion of this study is that transmission is maximized in the case of weak metal-nanotube coupling and extended contacts. In the case of metal contacts to graphitic carbon nanostructures, Pd appears to be the optimum contact metal as it has a similar work function as graphite and forms an epitaxial contact that is rather weak and causes only a minor perturbation of the electronic structure at the interface.

4.2.2. Optimizing metal contacts to transition metal dichalcogenides. Combining a layered structure and a nonzero fundamental band gap, nanostructures of transition metal dichalcogenides including molybdenum disulphide (MoS_2) have captured the interest of the scientific community [45]. These compounds consist of a metal layer sandwiched between two chalcogen (S, Se) layers. They are structurally very flexible and are being considered as a promising alternative to silicon- and carbon-based circuitry as well as molecular electronics [8, 46]. Bulk MoS_2, a well-established low-cost lubricant, has an indirect band gap of 1.2 eV [47] and a rather high carrier mobility [48, 49]. The initially reported electron mobility in single-layer MoS_2 has been very different from the bulk system [7, 8]. It is now agreed that the initial results have been adversely affected to some degree by the measurement technique [50, 51] and the assumption that the contact resistance can be neglected.

In reality, the contact resistance forms a significant part of the total resistance of the system and can not easily be neglected. If so, then the observed electron mobility may not represent an intrinsic property of the semiconducting single layer, as it would be biased by unfavorable contacts. As will be shown in the following, the contact resistance in this system is caused by a tunnel barrier that depends sensitively on the electronic structure at the MoS_2/metal interface [44].

Carrier injection from a metal into this semiconducting system can be understood by inspecting the electronic density of occupied and unoccupied states in a single-layer MoS_2, shown in figure 5. Aligning the Fermi level of MoS_2 with its work function $\Phi = 5.2\,\text{eV}$, we can clearly distinguish between suitable and less suitable contact metals. Since the energy gap has no states to tunnel to and the valence band is occupied, carrier injection from metals with a high work function including Pd and Au will be difficult to achieve. Most suitable contact metals for this system should have a low work function, which would enable injection into unoccupied states of the conduction band of MoS_2.

The electronic transparency of quantum contacts depends sensitively on a favorable interface geometry and bonding, the electronic density of states, and the potential barrier at the interface. Among transition metals with *d* orbitals that may

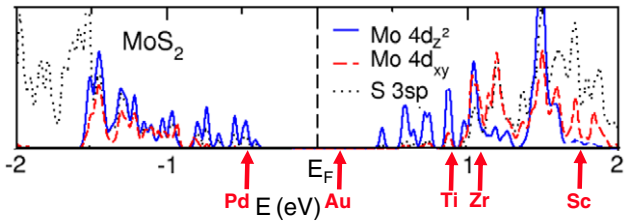

Figure 5. Partial electronic density of Mo and S states, which are relevant to bonding and charge injection, in the single-layer MoS_2. The position of the Fermi level of the system, aligned with the observed work function of 5.2 eV, is compared to the observed work functions of Au, Pd, Ti, Zr and Sc. Only a narrow energy region around the Fermi level E_F is shown. Adapted from [44]. Copyright 2012 by the American Physical Society.

favorably mix with Mo4*d* states, Sc, Ti and Zr emerge as suitable candidates. From the point of view of epitaxy, Sc and Zr are less suitable due to a large lattice mismatch, and Ti appears as an ideal candidate with only 1% mismatch to MoS_2.

The proper way to determine the electronic transparency of a contact is generally to perform a quantum transport calculation. For low bias voltages, the most common approach involves calculating the equilibrium Green's function, which to a large extent reflects the electronic density of states near E_F and the degree of delocalization of these states within the contact region. As seen in the DOS projection onto selected Mo and S orbitals in figure 5, states at bottom of the conduction band of single-layer MoS_2 are dominated by Mo4d_{z^2} orbitals, with the other Mo states playing only a minor role.

To illustrate the differences in bonding and electronic structure between single-layer MoS_2 and Au, Ti, Sc and Zr as contact metals, we show the equilibrium geometry and electronic structure at the interface in figure 6. Even though sulfur is generally known for its ability to form favorable thio bonds to Au, the sulfur at the surface of single-layer MoS_2 is fully saturated and does not bond strongly to Au. This is reflected in the large distance between the sulfur and the topmost Au layer in figure 6(*a*), which separates the Au contact and the Mo layer by 4.21 Å, far enough to suppress any efficient wavefunction overlap. The density of electrons in the energy range important for transport, depicted in the middle panel of figure 6(*a*), is very low at the interface between MoS_2 and Au, indicating that electron transport across the MoS_2/Au contact is mainly of tunneling nature. As seen in the right panel of figure 6(*a*), which depicts the averaged electrostatic potential, the contact tunnel barrier at the MoS_2/Au interface is formidable in height and width. It should be noted here that the general term 'tunnel barrier' appears more suited to describe the physical situation in this case than the commonly used term 'Schottky barrier', since the potential barrier is caused not only by charge transfer, but also by electronic structure changes due to covalent bonding.

As sulfur binds more strongly to Ti, the S and Ti layers are brought closer together, reducing the average Mo–Ti distance to 3.57 Å, as seen in figure 6(*b*). Thus, the overlap between energetically relevant wave functions of the Mo layer and the contact metal is significantly larger for Ti than for Au, as can be inferred by comparing the middle panels of figures 6(*a*) and (*b*). As a consequence, the tunnel barrier in this case is also lower. The same favorable situation occurs also at the MoS_2 interface with Sc and Zr, shown in figures 6(*c*) and (*d*).

The transmission coefficient for tunneling though a potential energy barrier can be estimated quantitatively using the WKB approximation from

$$|T(E)|^2 \approx \exp\left\{-2\int_{z_1}^{z_2}\left[(2m/\hbar^2)(V(z)-E)\right]^{1/2}\mathrm{d}z\right\}. \quad (4)$$

The tunneling current through a barrier depends not only on the transmission probability, but also the projected density of states N_p at both sides of the interface and is given by $I \propto T(E \approx E_F)\, N_p(MoS_2)\, N_p(\text{metal})$. Parameters characterizing the junction of MoS_2 with Au, Ti, Sc and Zr are summarized in table 1. The narrower and lower tunnel barriers in Ti, Sc and Zr increase the tunneling probability T between these metals and MoS_2 by a typical factor of 3–5 over Au as contact metal. Also the projections of the density of states at the Fermi level onto states of MoS_2 and the contact metal increase by a typical factor five each in contacts with Ti, Sc and Zr over Au contacts. This explains the net increase of the tunnel current I by two orders of magnitude when using Ti, Sc or Zr rather than Au contacts, with Sc providing the optimum contact. The superiority of Sc over Au as contact metal has been verified experimentally in the meantime [52].

The contact tunnel barriers can be lowered not only by a judicious choice of the contact metal, but also by externally modifying the electrostatic potential at the metal-semiconductor interface. This has been achieved successfully by surrounding the interface region by an ionic liquid [53, 54]. The beneficial effect of the effective screening of the electric field at the interface by liquid ion gating was the elimination of the contact resistance as an important obstacle to a direct observation of the intrinsic, phonon-limited carrier mobility. Even though ionic liquids are unlikely to be used for practical applications, they are well suited to judge the quality of optimized contacts.

5. Blessings of incommensurability

Lack of commensurability or epitaxy between a 2D overlayer and the substrate is generally considered detrimental to the quality of the interface, as will be discussed in section 6. In specific cases, however, lack of epitaxy may turn to a blessing. To accommodate its lattice mismatch with a given substrate, a mechanically flexible overlayer—such as graphene—may optimize its adhesion to the substrate by forming a periodic wavy structure that is unrelated to either side of the interface. In systems such as layered phosphorus with many different allotropes, a judicious choice of the substrate may suppress the formation of unwanted allotropes during CVD growth. Finally, designer superlattices of grain boundaries that may grow on specifically prepared incommensurate substrates could modify thermal and electrical transport in a desirable way.

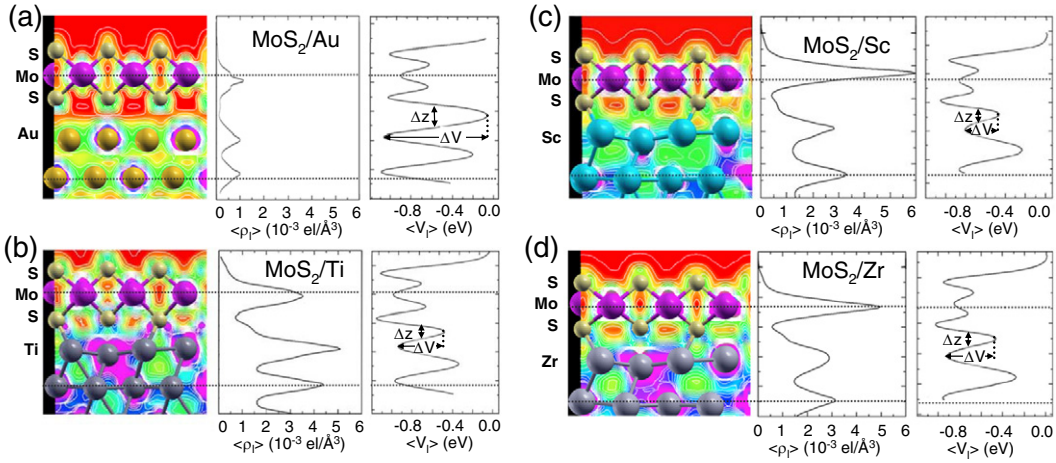

Figure 6. Electronic structure at the interface between MoS_2 and (*a*) Au, (*b*) Ti, (*c*) Sc and (*d*) Zr. Left panels display contour plots of the electron density ρ_l associated with states in the energy range $E_F - 0.1\,\text{eV} < E < E_F + 0.1\,\text{eV}$ in planes normal to the interface, superposed with the atomic positions. Middle panels display the average value of $\langle\rho_l\rangle(z)$ and right panels the average electrostatic potential $\langle V_l\rangle(z)$ in $z = \text{const.}$ planes parallel to the interface. The height ΔV and the width Δz of the tunnel barrier are indicated in the right panels. (*a*) and (*b*) adapted from [44]. Copyright 2012 by the American Physical Society. (*c*) and (*d*) courtesy of Gotthard Seifert and Igor Popov.

Table 1. Parameters affecting the transparency of contacts between MoS_2 and selected transition metals, depicted in figure 6.

System	Barrier width (Å)	Barrier height (eV)	$T/T_{\min}$	N_p (MoS_2) (states/eV)	N_p (metal) (states/eV)	$I/I_{\min}$
MoS_2/Au	1.59	1.03	1.0	1.4	7.2	1
MoS_2/Ti	0.90	0.45	3.7	7.5	39.1	105
MoS_2/Sc	0.87	0.34	4.2	7.6	37.8	117
MoS_2/Zr	0.97	0.45	3.6	8.0	37.5	103

Note: Barrier widths are taken at half height of the potential barrier between MoS_2 and the contact metal. N_p is the projection of the density of states at E_F onto states of either MoS_2 or the contact metal. $T/T_{\min}$ is the relative transparency of the contact and $I/I_{\min}$ is the expected relative increase in the tunnel current at small bias voltages.

5.1. Wavy graphene: escaping into the third dimension

Even though silicon and carbon are very similar in many ways, graphene is not epitaxial with any silicon surface. One possible way to achieve epitaxy on the Si(100) surface is by in-plane compression of the graphene layer [55], which would come at a high energy cost resulting in spontaneous delamination. Also at the Si(1 1 1) surface with the same sixfold symmetry as the graphene overlayer, there is a large 11.6% lattice mismatch, which needs to be accommodated in a different way than by in-layer compression.

Owing to its limited flexural rigidity, graphene may accommodate the lattice mismatch by buckling and transforming to a wavy structure shown in figure 7(*a*) [56]. In this case, the structure of the graphene overlayer is an energetic compromise between maximizing the number of covalent graphene-silicon bonds, which favors a short wavelength a_1, and minimizing the bending energy, which favors a long wavelength. The optimum 2×1 superlattice structure in figure 7(*a*) represents such an energy compromise. By its origin, this structure is very different from thermodynamically induced rippling observed in graphene on metal substrates [57]. As seen in figure 7(*c*), a very similar structure can form, for the same reason, at the interface between the (1 1 1) surface of cubic diamond and graphene [58].

The major benefit of the wavy structure is the coexistence of ribbon-shaped conducting graphene ridges that are detached from the substrate and separated by ribbons of carbon atoms bonded covalently to the substrate, enabling carrier injection across the interface. This best seen in the top view of the structures, shown in figure 7(*b*) for graphene on Si(1 1 1) and in figure 7(*d*) for graphene on the C(1 1 1) diamond surface. On Si(1 1 1), the detached graphene ridges that are highlighted in figure 7(*b*) contain embedded paraphenylene chains partly resembling poly-perinaphtalene. The separating regions contain sp^3 carbon atoms covalently connected to the Si substrate and short carbon chains resembling butadiene. On C(1 1 1), the detached ridges resemble polyacetylene chains that are not dimerized due to steric constraints imposed by the embedding lattice.

Of importance for transport properties is the fact that both the paraphenylene chains on Si(1 1 1) and polyacetylene chains on C(1 1 1) are sufficiently separated and thus mearly decoupled from the substrate. Since both paraphenylene and polyacetylene chains are conducting, they may be considered an array of parallel quantum wires. These quantum wires are separated by carbon atoms in the graphene layer that bond covalently to the substrate by forming strong sp^3 bonds. Since sp^3 hybridized carbon, found in diamond, is associated with insulating behavior, we may expect that the partly decoupled quantum wires may dominate transport in the overlayer. The emergence of quasi-1D substructures in the 2D lattice of graphene gives rise to van Hove singularities in the density of states that, in turn, affect conductance.

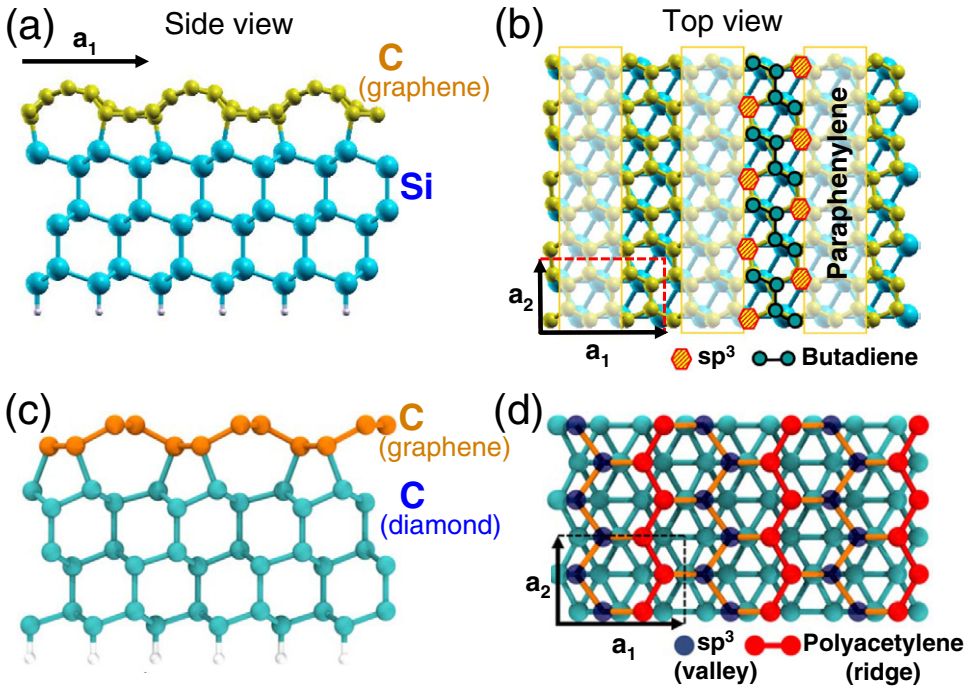

Figure 7. Optimum geometry of wavy graphene on the (1 1 1) surfaces of Si (*a*), (*b*) and diamond (*c*), (*d*). The side view of graphene/Si(1 1 1) in (*a*) and graphene/C(1 1 1) in (*c*) shows, how incommensurability along the a_1 direction can be accommodated by graphene assuming a wavy structure. The top view of graphene/Si(1 1 1) in (*b*) allows a distinction between ridges of C atoms forming paraphenylene chains, which can be distinguished from sp^3 C atoms covalently bonded to Si and C atoms in butadiene like units that are not covalently bonded to Si. Similarly, the top view of graphene/C(1 1 1) in (*d*) allows to distinguish ridges of free-standing C atoms in graphene, which form polyacetylene chains from sp^3 C atoms covalently bonded to the diamond surface. a_1 and a_2 are the Bravais lattice vectors defining the 2×1 unit cell of the substrate. (*a*), (*b*) adapted from [56]. Copyright 2013 by the American Physical Society. (*c*), (*d*) adapted from [58].

Results of quantum transport studies of wavy graphene on Si(1 1 1) are summarized in figure 8. The schematic structure, depicted in figure 8(*a*), distinguishes the transport direction *A* parallel to the ridges from direction *B* normal to the ridges. Transmission spectra $G(E)$ of a contiguous graphene layer in different environments are shown in figure 8(*b*) for transport geometry *A* and in figure 8(*c*) for transport geometry *B*. In both cases, we compare the quantum conductance of wavy graphene in contact to Si(1 1 1) to that of a free-standing wavy or a planar graphene monolayer.

Maybe the most unexpected result is the calculated quantum conductance in transport geometry *A*, shown in figure 8(*b*). The transmission spectrum of wavy graphene displays more peaks than that of planar graphene, reflecting changes in the density of states. Comparison between the dashed red and the dotted blue line indicates that the mere effect of rippling increases the conductance along the ridges of a free-standing graphene monolayer significantly. Depositing the rippled graphene monolayer onto the substrate lowers conductance by introducing new scattering centers. Still, within 0.5 eV of the Fermi level, the conductance of the wavy graphene layer on Si(1 1 1) exceeds that of a free-standing graphene monolayer.

Our results in figure 8(*c*) indicate that transmittance normal to the graphene ridges is reduced when compared to planar graphene. The transmission spectrum of a free-standing wavy graphene monolayer contains a narrow transport gap of $\lesssim$0.05 eV. Si acts as a weak scatterer when connected to wavy graphene, which further reduces the conductivity of the wavy graphene layer and opens an ≈0.35 eV wide transport gap.

The conducting behavior at the C(1 1 1) diamond surface covered by a wavy graphene monolayer [58] is very similar to that found on the related Si(1 1 1) substrate. Results in figure 8 for transport geometries *A* and *B* confirm the above mentioned hypothesis about the formation of anisotropic preferential transmission channels in wavy graphene, which are responsible for conduction enhancement along the conductive ridges and suppression of conduction normal to these ridges.

5.2. Using epitaxy for allotrope selection

Layered phosphorus structures that are related to black phosphorus [60, 61] are emerging as viable contenders in the competitive field of two-dimensional semiconductors [62, 63]. Most studies report observations of few-layer phosphorene structures that have been mechanically exfoliated from black phosphorus. In contrast to semimetallic graphene, few-layer phosphorene displays a significant band-gap while still maintaining a higher carrier mobility than transition metal dichalcogenides [3, 9, 64]. Interest in few-layer phosphorene is rising rapidly, since the fundamental band gap is tunable in a wide range by the number of layers and by in-layer strain [3–6]. Even more intriguing is the (so far theoretical) postulate of other layered phosphorene allotropes shown in figure 9, including blue P, γ-P and δ-P, which are nearly as stable as black P, but differ in their electronic structure [4, 59, 65].

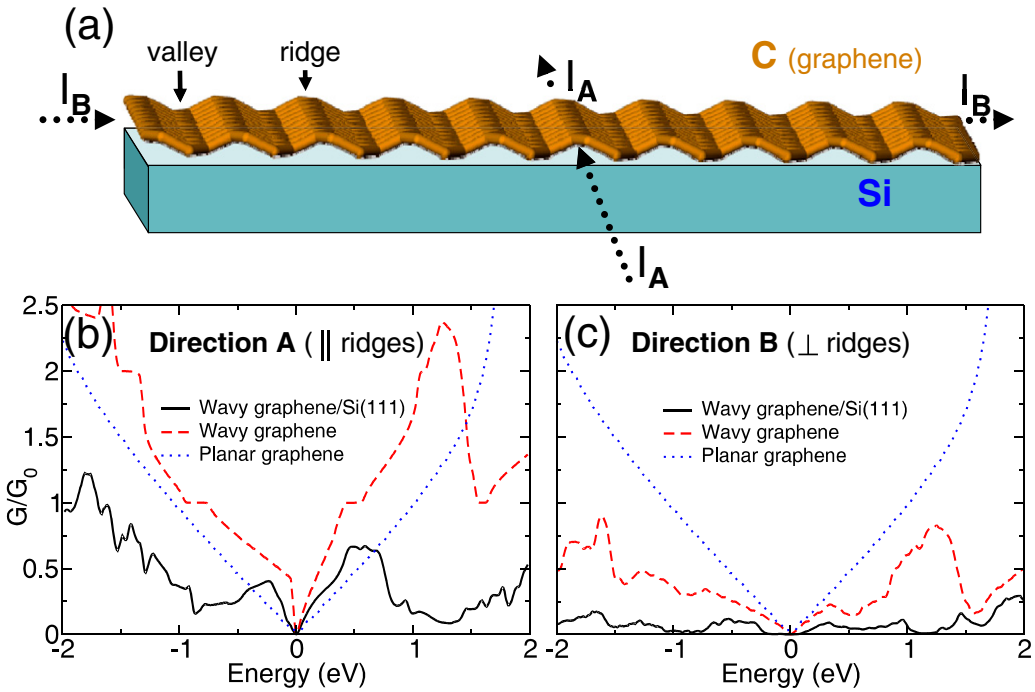

Figure 8. (*a*) Perspective view of graphene on Si(1 1 1), illustrating the transport direction along the ridges (*A*) and normal to the ridges (*B*). Quantum conductance *G* along (*b*) and normal to the ridges (*c*) in units of the conduction quantum G_0 as a function of injection energy, with $E = 0$ corresponding to zero bias. The conductance is given per unit cell normal to the transport direction. (*a*) adapted from [58]. (*c*), (*d*) adapted from [56]. Copyright 2013 by the American Physical Society.

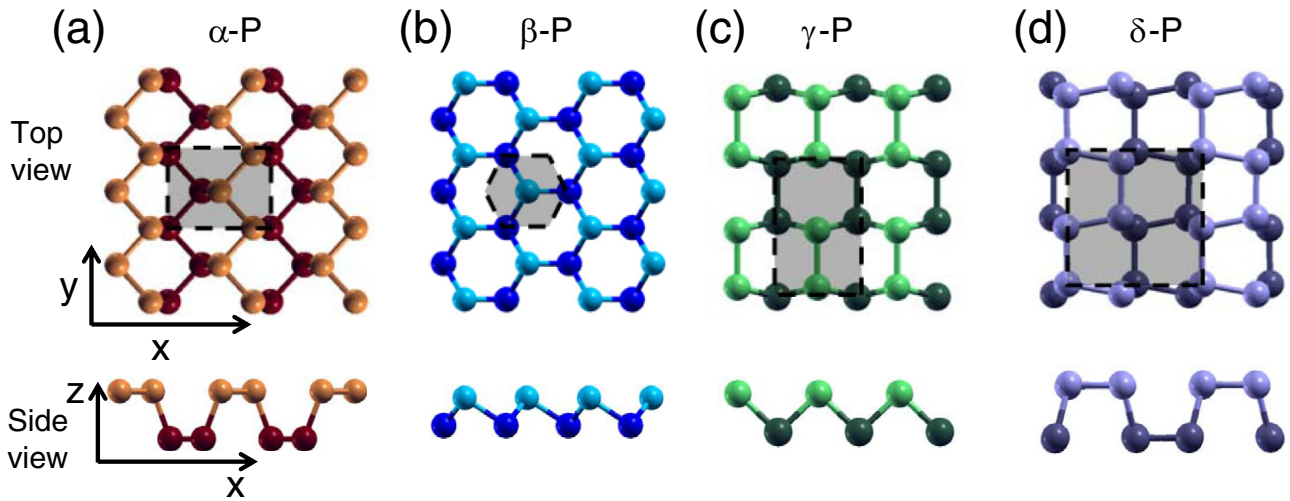

Figure 9. Equilibrium structure of (*a*) an α-P (black), (*b*) β-P (blue), (*c*) γ-P and (*d*) δ-P monolayer in both top and side views. Atoms at the top and bottom of the non-planar layers are distinguished by color and shading and the Wigner–Seitz cells are shown by the shaded regions. Reproduced with permission from [59]. Copyright 2014 by the American Physical Society.

Unlike in most other systems, different allotropes of phosphorus are predicted to coexist within a monolayer with virtually no energy penalty to form domain boundaries [59, 66, 67]. Even though only layered blue phosphorus has been identified experimentally as the *A*7 phase [68] of bulk phosphorus, it is likely that other phases may be present in monolayers produced by chemical vapor deposition or molecular beam epitaxy, which had been successfully used to produce few-layer arsenene [69]. If so, then a judicious choice of a single-crystal substrate may not only allow to select the preferential allotrope that should form during CVD or MBE growth, but also design a pre-determined complex pattern of coexisting allotropes. This approach may allow to form multi-phase phosphorene layers with a complex conduction pattern. Since pristine phosphorus is rather unstable in air, protection from oxidation is essential; this can be achieved by capping the monolayer by a monolayer of hexagonal boron nitride [61]. It is interesting to realize that the atomic structure of the underlying phosphorene monolayer can be identified by tunneling through the protective *h*-BN monolayer in an STM study [70].

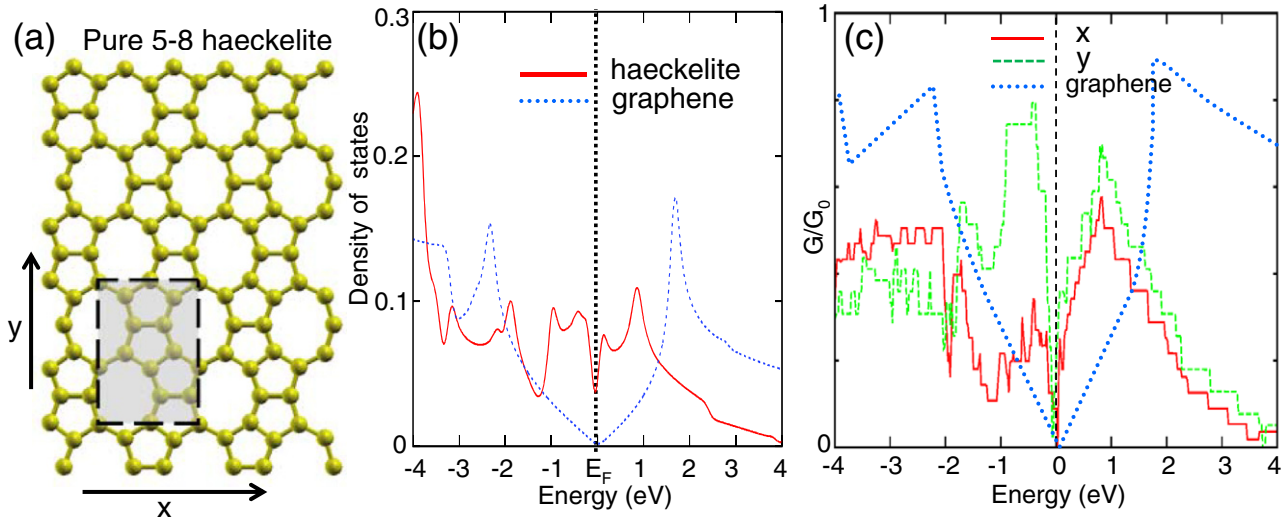

Figure 10. (a) Atomic structure, (b) electronic density of states and (c) quantum conductance G of a 5–8 haeckelite monolayer. The conductance is given per unit cell normal to the transport direction. Results for a pristine graphene monolayer are indicated by the dotted blue lines for simple comparison. Adapted from [71].

5.3. Enhancing electrical conductance at grain boundaries

Most important structural defects are grain boundaries. Grain boundaries are a non-desired by-product of the layer growth process or may form in order to relieve strain caused by structural mismatch at the interface. Whereas presence of defects such as grain boundaries generally deteriorates conductance, there are a few exceptions, where the opposite is the case.

Presence of defect-induced localized states near the Fermi level is known to enhance electrical conductance not only in semiconductors like MoS_2 [72], but also in semi-metals like graphene with a low density of states near E_F. Under some conditions, the increase in the electronic density of states near the Fermi level may benefit the conductance in the diffusive regime more than losses caused by the reduced electron mean free path. Structural defects are a natural side effect of the efficient CVD process that has been developed to grow large-area graphene [11–14, 16]. Typical defects in CVD-grown graphene are arrays of non-hexagons rings along grain boundaries [16]. Highly defective graphitic structures resemble haeckelites [73, 74], which are ordered sp^2 bonded carbon structures with not only hexagonal rings. In comparison to a defect-free graphene monolayer, all these structures display an enhanced density of states near the Fermi level [71].

The equilibrium geometry, electronic density of states and quantum conductance in a free-standing monolayer of 5–8 haeckelite are shown in figure 10. The main relation between haeckelite and graphene is the planarity of these sp^2 bonded structures and the fact that all atoms are threefold coordinated. Whereas the density of states in semimetallic graphene is strictly zero at E_F, the density of states of the haeckelite structure in figure 10(b) displays only a narrow pseudogap at the Fermi level. In contrast to the isotropic conductance behavior in pristine graphene, the conductance of a haeckelite monolayer, shown in figure 10(c), is enhanced near E_F, but is strongly anisotropic.

A model geometry of CVD-grown graphene containing regions of pristine graphene connected by non-hexagonal rings is shown in figure 11. In the h-(n, m) structures depicted in figures 11(a)–(c), n-hexagon wide zigzag graphene nanoribbons are connected by m-octagon wide 5–8 haeckelite strips at the grain boundary. The structure can be changed from pure 5–8 haeckelite, defined by $n = 0$ and depicted in figure 10, to pristine graphene for $n \to \infty$. The structure with the narrowest graphene strips, h-$(2, 2)$ in figure 11(a), differs most from both graphene and 5–8 haeckelite. Its density of states $N(E)$ in figure 11(d) displays a maximum at the Fermi level, which is very different from $N(E_F) = 0$ in graphene and the pseudogap at E_F of the haeckelite in figure 10(b). This nonzero density of states increases the quantum conductance in the same energy range, as seen in figure 11(g). Comparison between figures 11(d)–(f) reveals that the prominent maximum in the density of states near E_F recedes with increasing width of the graphene nanoribbons. The increasing similarity of h-(n, m) structures with increasing n and graphene is also reflected in the quantum conductance, shown in figures 11(g)–(i). In systems with very wide graphene nanoribbons, the conductance at E_F will eventually be dominated by defect bands along the haeckelite-graphene grain boundary, which will act as quantum wires. Defects like these thus enhance the conductance of pristine semimetallic graphene.

6. Curses of incommensurability

As mentioned above, formation of defects including grain boundaries [16] is a common side effect of the CVD growth process kinetics [11–14, 16] that can be controlled to some degree. Grain boundaries are also a means to accommodate lattice mismatch and reduce strain at the interface between a 2D structure and an incommensurate substrate, which can not be avoided except by changing the substrate. Defects are scattering centers that reduce conductance by reducing the

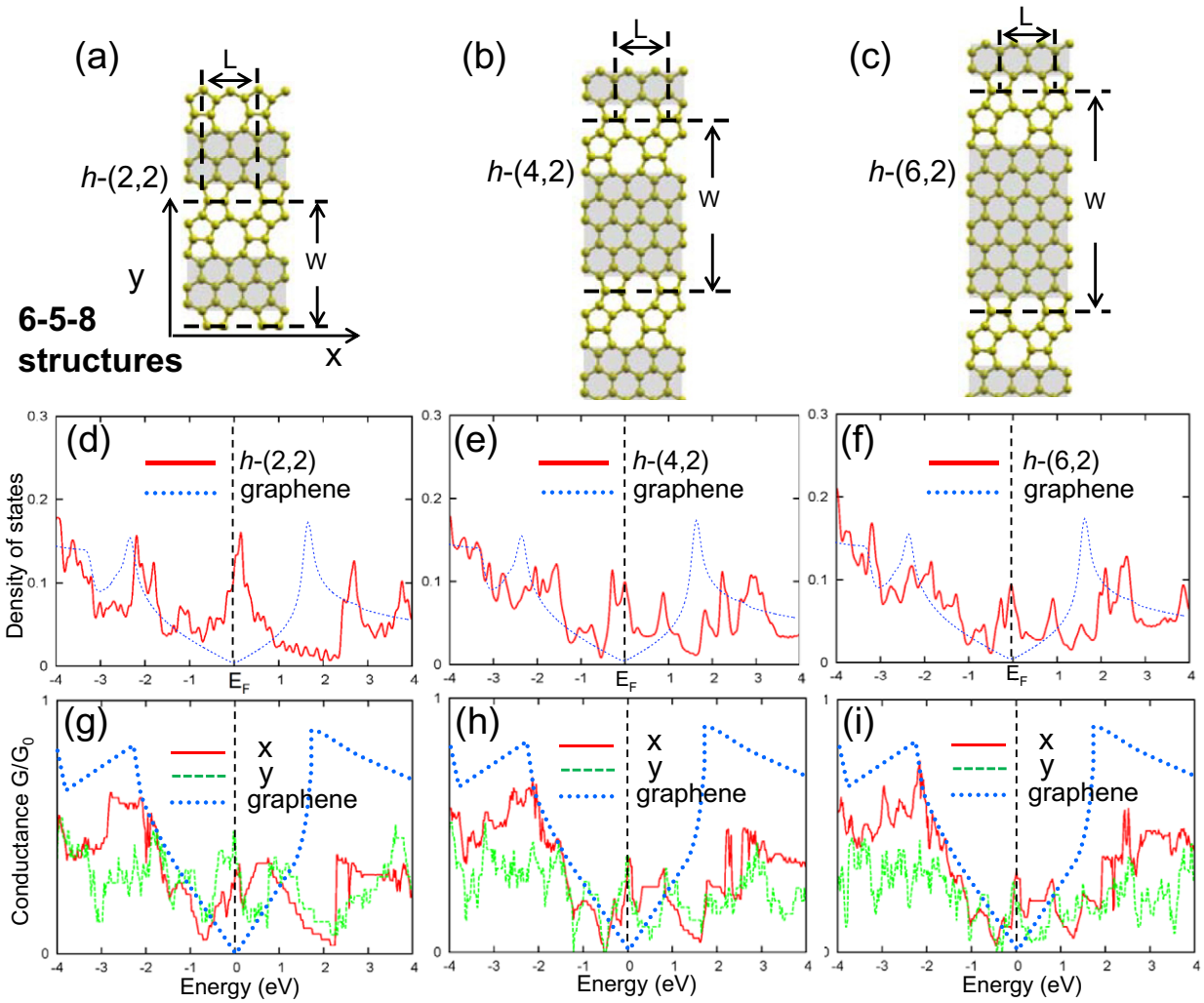

Figure 11. Electronic properties of h-(n, m) hybrid monolayers consisting of alternating zigzag graphene nanoribbons with n rows of hexagons and strips containing m rows of 5–8 haeckelite. Graphitic portions in the $L \times W$ unit cells are enhanced by grey shading in the ball-and-stick models in (a)–(c). (d)–(f) Electronic density of states and (g)–(i) quantum conductance G along and perpendicular to the direction of the grain boundaries. Results for a pristine graphene monolayer are indicated by the dotted blue lines for simple comparison. Adapted from [71].

electron and phonon mean free path and by blocking particular conduction channels.

An essential prerequisite for nonzero conductance between two points is their connection by a percolating path allowing the propagation of charges or phonons. Defects, which cut all percolation paths, stop all transport even though the material itself may be a perfect conductor. This is trivially obvious in a copper wire cut in half, which does not conduct in spite of a non-vanishing electronic density of states at the Fermi level. Even though isolated defects do not completely disrupt a percolation path between two points, they still can significantly degrade the net conductance of a structure.

6.1. Reduction of the electrical conductance by defects and grain boundaries

For a completely disrupted 2D layer, only a significant contact with a substrate may restore thermal and heat transport. This has been shown in the case of incommensurate graphene interfacing the Si(1 1 1) surface, presented in figure 12. Clearly, a free-standing graphene monolayer that is torn apart does not conduct. As seen in figure 12(c), only a sufficient contact between the disrupted wavy graphene overlayer and the silicon substrate may restore at least a small fraction of the initial conductance of the pristine graphene monolayer by providing a possibility to inject carriers from graphene to silicon and back and thus bridge the extended defect [56].

6.2. Defect-related reduction of the thermal conductance

Defects in a 2D layer deteriorate not only transport of charge, but also of heat, the key to efficient thermal management. Phonons scatter not only from structural defects, but also from isotopic impurities. This latter aspect should not be overlooked in layered structures of low-Z elements such as graphene. It is known that the 8% deviation from unity in the $^{13}C/^{12}C$ mass ratio reduces the thermal conductivity of diamond [75, 76] and graphitic structures [77, 78] with an isotope mixture by up to one half. The adverse effect of isotopic impurities and structural defects is shown in figure 13, which depicts

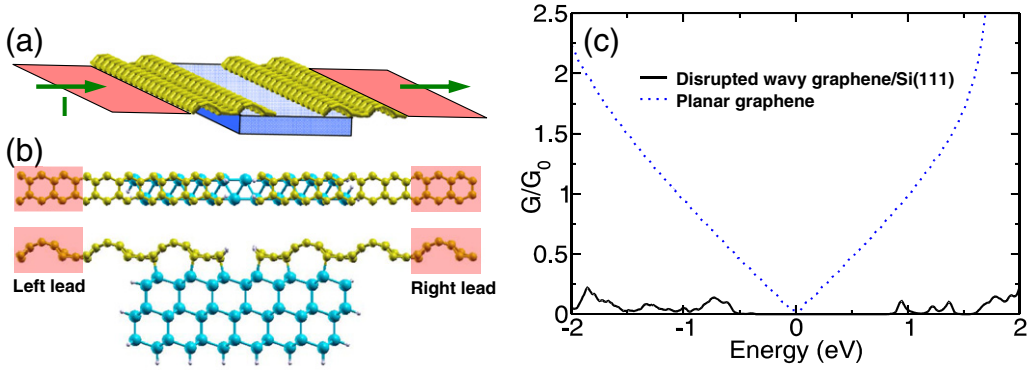

Figure 12. Geometry and quantum transport calculation for a disrupted wavy graphene layer bonded to Si(1 1 1). Except for the removal of a ridge in the scattering region, the transport geometry is analogous to that of direction B in figure 8. (a) Schematic geometry for the calculation, distinguishing free-standing perfect graphene leads from the central scattering region, with the direction of the current I shown by the arrow. (b) Atomic structure of the scattering region and its connection to the leads in top and side view. (c) Quantum conductance G in units of the conduction quantum G_0 as a function of injection energy, with $E = 0$ corresponding to the Fermi level. The conductance is given per unit cell normal to the transport direction, shown in panel (b). Adapted from [56]. Copyright 2013 by the American Physical Society.

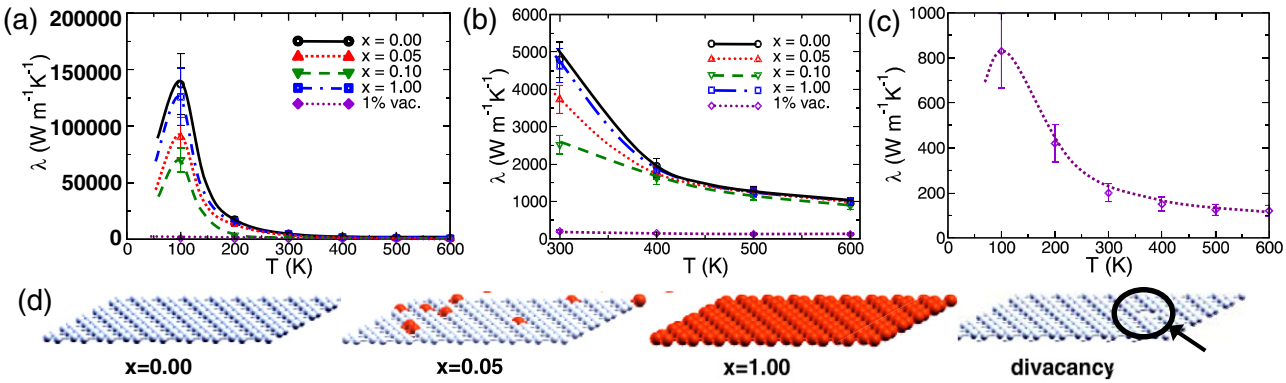

Figure 13. Thermal conductivity λ of perfect and defective graphene as a function of temperature T. (a) λ in $^{13}C_x{}^{12}C_{1-x}$ graphene with varying isotopic composition in comparison to pure ^{12}C graphene with 1% missing atoms forming divacancy defects. (b) Details of (a) on a reduced temperature scale. (c) λ of ^{12}C graphene with divacancies, presented in (a) and (b), on an expanded λ scale. (d) Depiction of the graphene unit cells containing different types of defects. The lines in (a)–(c) are guides to the eye. Reproduced with permission from [79]. Copyright 2012 by the American Physical Society.

the temperature dependence of the thermal conductivity of defective graphene [79].

The phonon component of the thermal conductivity λ, which is dominant in all-carbon systems like graphene or diamond, is the product of the specific heat per volume, the speed of sound, and the phonon mean free path. The temperature dependence of the thermal conductivity is dominated by the specific heat approaching zero for $T \to 0$ and the phonon mean free path decreasing to zero for $T \to \infty$. Rigid interatomic bonds in both sp^2 and sp^3 carbon structures are responsible for a very high speed of sound and hard phonon modes, which translate into a high Debye frequency associated with a large value of the specific heat. In isotopically pure monocrystalline diamond and graphitic nanostructures, the phonon mean free path may approach a large fraction of a micrometer, giving rise to record thermal conductivity values [75, 81, 82] as large as $\lambda \approx 40\,000\,\mathrm{Wm^{-1}\,K^{-1}}$ near $T \approx 100\,\mathrm{K}$.

Since presence of isotopic or structural impurities has little effect on the speed of sound or on specific heat, defect-related reduction of the thermal conductivity in graphene monolayers, reproduced in figure 13, is mostly caused by the decrease in the phonon mean free path. Results presented in figure 13(a) and (b) for structurally perfect graphene with the isotopic composition $^{13}C_x{}^{12}C_{1-x}$ support this interpretation, since the thermal conductivity in pure ^{13}C monolayer is indistinguishable from that in ^{12}C within the error bars. These computational results also reflect the observed significant reduction of the thermal conductivity in isotopically impure samples.

Results in figure 13(a) and (b) also demonstrate that even a low concentration of divacancies quenches thermal conductivity more significantly than isotopic impurities in structurally perfect graphene. As seen in figure 13(c), $\lambda(T)$ in graphene with divacancies keeps the same general shape, but is significantly lower than in a structurally perfect lattice. A common type of defects in graphitic structures are Stone-Wales defects, shown in figure 14(a), which are caused by a mere bond rotation. Data in figure 14(b) indicate that even though these defects keep all atoms threefold coordinated, they reduce thermal transport in a similar way as divacancies [80].

In analogy to charge transport discussed above, extended or line defects cause the most drastic reduction in thermal

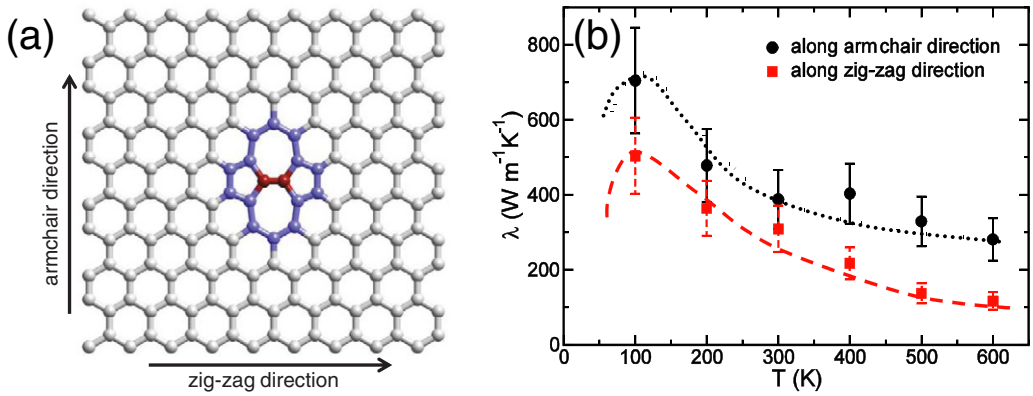

Figure 14. Thermal conductivity of a graphene monolayer with a single 5775 defect, created by a 90° rotation of one bond highlighted in dark red. (*a*) The 180-atom unit cell used in the computer simulation. Atoms in the defect region are emphasized by darker (blue) color. (*b*) Thermal conductivity λ as a function of temperature T for thermal transport along the zig-zag and armchair direction, shown in (*a*). Lines connecting the data points are guides to the eye. Adapted from [80]. Copyright 2014 by the American Physical Society.

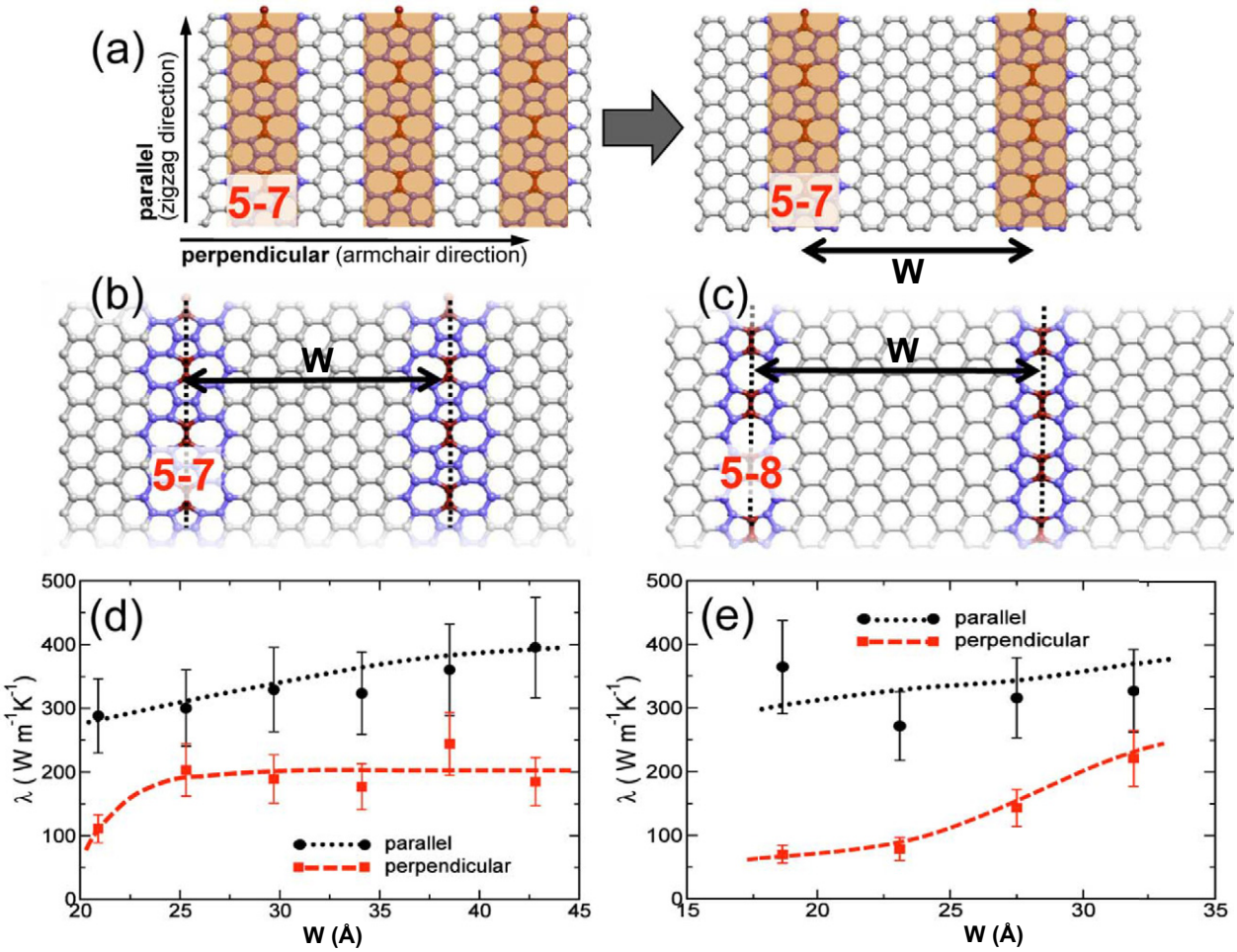

Figure 15. Effect of line defects on the thermal conductivity of a graphene monolayer. (*a*) Arrangement of 5–7 defect lines, highlighted by shading, which separate graphene strips of width W, and the definition of thermal transport directions. Equilibrium structure of (*b*) 5–7 and (*c*) 5–8 defect lines, separated by the distance W. Atoms in non-hexagonal rings are emphasized by the darker color. Bonds rotated by 90° are enhanced by dark red. Thermal conductivity λ of the system with (*d*) 5–7 and (*e*) 5–8 line defects as a function of their separation W at $T = 300$ K. Data points for transport parallel and perpendicular to the line defects are connected by dashed and dotted lines, respectively, as guides to the eye. Adapted from [80]. Copyright 2014 by the American Physical Society.

conductivity. In graphene grown on an incommensurate substrate, such line defects are found at grain boundaries. Thermal transport results in hybrid structures consisting of graphene nanoribbons separated by lines of 5–7 or 5–8 defects, similar to those observed in defective graphene [16], are shown in figure 15. Similar to figure 11, the hybrid structures will reduce to graphene for $W \to \infty$. As expected, the calculated thermal conductance shown in figures 15(*d*) and (*e*)

is larger along the graphene nanoribbons than normal to the nanoribbons, in which case scattering at the grain boundaries can not be avoided. Comparison between figures 15(*d*) and (*e*) indicates that, within the error bars, the precise structure of the grain boundaries does not matter much. Quantitative comparison with room temperature data for a perfect ^{12}C graphene layer in figure 13(*b*) indicates that thermal conductance along the direction of graphene nanoribbons is significantly reduced by grain boundary scattering and that λ approaches the record value of a defect-free graphene monolayer very slowly with increasing ribbon width.

7. Summary and conclusions

This topical review provides a non-exhaustive summary of important issues worth considering when attempting to integrate 2D nanostructures within the current 3D technology. The significant role of the surface energy in ultra-thin films causes fundamental structural changes, including graphitization, in a wide range of compounds with a bulk cubic structure, which in turn changes their physical properties. The exceptional electrical and thermal conductance of 2D materials such as graphene or transition metal dichalcogenides is affected significantly by the nature of the interface with the substrate or a metal contact. Electrical contacts to 2D nanostructures must be understood as genuine quantum devices. Electronic transparency of such contacts, which underlies the contact resistance, depends sensitively on favorable interface geometry and bonding, the electronic density of states and Fermi velocity on both sides of the contact, as well as a tunneling barrier that may form at the interface. Contact optimization involving all these aspects is a crucial prerequisite for improving the performance of a composite device. Defects, in particular line defects at grain boundaries caused by growth kinetics or as a side effect of structural incommensurability, are usually detrimental to charge and heat transport, since they reduce the mean-free path of the carriers. Specific changes in epitaxy may also be used for allotrope selection or allotrope patterning, such as in ultrathin phosphorene films. Lack of epitaxy may cause a desired transformation from isotropic to a distinct anisotropic conductance behavior in a 2D layer. This is the case in the wavy graphene structure that may form on Si(1 1 1), or in single-crystal grains within a 2D overlayer that display a preferential anisotropy. Ignoring the key role of the 2D/3D interface and of defects in low-dimensional structures may cause serious errors in judging the performance of 2D nanostructures in a 3D environment.

Acknowledgment

This study has been supported by the National Science Foundation Cooperative Agreement #EEC-0832785, titled 'NSEC: Center for High-rate Nanomanufacturing'. I acknowledge fruitful discussions with I Baburin, M Baldoni, G Cuniberti, Z Fthenakis, J Guan, A G Kvashnin, S Leoni, N Nemec, I Popov, G Seifert, D Selli, P B Sorokin, C Tayran, P D Ye, Z Zhou and Z Zhu, who contributed significantly to this work.

References

[1] Novoselov K S, Geim A K, Morozov S V, Jiang D, Zhang Y, Dubonos S V, Grigorieva I V and Firsov A A 2004 *Science* **306** 666–9
[2] Bolotin K, Sikes K, Jiang Z, Klima M, Fudenberg G, Hone J, Kim P and Stormer H 2008 *Solid State Commun.* **146** 351–5
[3] Liu H, Neal A T, Zhu Z, Luo Z, Xu X, Tomanek D and Ye P D 2014 *ACS Nano* **8** 4033–41
[4] Zhu Z and Tománek D 2014 *Phys. Rev. Lett.* **112** 176802
[5] Rodin A S, Carvalho A and Castro Neto A H 2014 *Phys. Rev. Lett.* **112** 176801
[6] Fei R and Yang L 2014 *Nano Lett.* **14** 2884–9
[7] Novoselov K S, Jiang D, Schedin F, Booth T J, Khotkevich V V, Morozov S V and Geim A K 2005 *Proc. Natl Acad. Sci. USA* **102** 10451–3
[8] Radisavljevic B, Radenovic A, Brivio J, Giacometti V and Kis A 2011 *Nat. Nanotech.* **6** 147–50
[9] Li L, Yu Y, Ye G J, Ge Q, Ou X, Wu H, Feng D, Chen X H and Zhang Y 2014 *Nat. Nanotech.* **9** 372–7
[10] Boehm H P, Clauss A, Hofmann U and Fischer G O 1962 *Z. Naturforsch.* B **17** 150 (http://zfn.mpdl.mpg.de/data/Reihe_B/17/ZNB-1962-17b-0150.pdf)
[11] Wei D, Liu Y, Wang Y, Zhang H, Huang L and Yu G 2009 *Nano Lett.* **9** 1752–8
[12] Reina A, Jia X, Ho J, Nezich D, Son H, Bulovic V, Dresselhaus M S and Kong J 2009 *Nano Lett.* **9** 30
[13] Kim K S, Zhao Y, Jang H, Lee S Y, Kim J M, Kim K S, Ahn J H, Kim P, Choi J Y and Hong B H 2009 *Nature* **457** 706–10
[14] Li X *et al* 2009 *Science* **324** 1312–4
[15] Song L *et al* 2010 *Nano Lett.* **10** 3209–15
[16] Huang P Y *et al* 2011 *Nature* **469** 389–92
[17] Sorokin P B, Kvashnin A G, Zhu Z and Tomanek D 2014 *Nano Lett.* **14** 7126–30
[18] Banhart F 1999 *Rep. Prog. Phys.* **62** 1181–221
[19] Shang N, Papakonstantinou P, Wang P, Zakharov A, Palnitkar U, Lin I N, Chu M and Stamboulis A 2009 *ACS Nano* **3** 1032–8
[20] Kvashnin A, Chernozatonskii L A, Yakobson B I and Sorokin P B 2014 *Nano Lett.* **14** 676–81
[21] Lin S S 2012 *J. Phys. Chem.* C **116** 3951–5
[22] Claeyssens F, Freeman C L, Allan N L, Sun Y, Ashfold M N R and Harding J H 2005 *J. Mater. Chem.* **15** 139–48
[23] Singh A K, Zhuang H L and Hennig R G 2014 *Phys. Rev.* B **89** 245431
[24] Feng B, Ding Z, Meng S, Yao Y, He X, Cheng P, Chen L and Wu K 2012 *Nano Lett.* **12** 3507–11
[25] Vogt P, De Padova P, Quaresima C, Avila J, Frantzeskakis E, Asensio M C, Resta A, Ealet B and Le Lay G 2012 *Phys. Rev. Lett.* **108** 155501
[26] Lin C L, Arafune R, Kawahara K, Tsukahara N, Minamitani E, Kim Y, Takagi N and Kawai M 2012 *Appl. Phys. Express* **5** 045802
[27] Fleurence A, Friedlein R, Ozaki T, Kawai H, Wang Y and Yamada-Takamura Y 2012 *Phys. Rev. Lett.* **108** 245501
[28] Meng L, Wang Y, Zhang L, Du S, Wu R, Li L, Zhang Y, Li G, Zhou H, Hofer W A and Gao H J 2013 *Nano Lett.* **13** 685–90
[29] Zhang Z, Zeng X C and Guo W 2011 *J. Am. Chem. Soc.* **133** 14831–8
[30] Odkhuu D, Shin D, Ruoff R S and Park N 2013 *Sci. Rep.* **3** 3276
[31] Zhuang H L and Hennig R G 2014 *JOM* **66** 366–74
[32] Léonard F and Talin A A 2006 *Phys. Rev. Lett.* **97** 026804
[33] Lin Y F and Jian W B 2008 *Nano Lett.* **8** 3146–50
[34] Landman U, Barnett R N, Scherbakov A G and Avouris P 2000 *Phys. Rev. Lett.* **85** 1958–61

[35] Nemec N, Tomanek D and Cuniberti G 2006 *Phys. Rev. Lett.* **96** 076802
[36] Iijima S 1991 *Nature* **354** 56–8
[37] Tans S J, Devoret M H, Dai H, Thess A, Smalley R E, Geerligs L J and Dekker C 1997 *Nature* **386** 474–7
[38] Bockrath M, Liang W, Bozovic D, Hafner J H, Lieber C M, Tinkham M and Park H 2001 *Science* **291** 283–5
[39] Yaish Y, Park J Y, Rosenblatt S, Sazonova V, Brink M and McEuen P L 2004 *Phys. Rev. Lett.* **92** 046401
[40] Liang W, Bockrath M, Bozovic D, Hafner J H, Tinkham M and Park H 2001 *Nature* **411** 665–9
[41] Wakaya F, Katayama K and Gamo K 2003 *Microelectron. Eng.* **67-68** 853–7
[42] Javey A, Guo J, Wang Q, Lundstrom M and Dai H 2003 *Nature* **424** 654–7
[43] Mann D, Javey A, Kong J, Wang Q and Dai H 2003 *Nano Lett.* **3** 1541–4
[44] Popov I, Seifert G and Tománek D 2012 *Phys. Rev. Lett.* **108** 156802
[45] Tenne R, Margulis L, Genut M and Hodes G 1992 *Nature* **360** 444
[46] Yoon Y, Ganapathi K and Salahuddin S 2011 *Nano Lett.* **11** 3768–73
[47] Kam K K and Parkinson B A 1982 *J. Phys. Chem.* **86** 463–7
[48] Fivaz R and Mooser E 1967 *Phys. Rev.* **163** 743–55
[49] Podzorov V, Gershenson M E, Kloc C, Zeis R and Bucher E 2004 *Appl. Phys. Lett.* **84** 3301
[50] Fuhrer M S and Hone J 2013 *Nat. Nano.* **8** 146–7
[51] Radisavljevic B and Kis A 2013 *Nat. Nano.* **8** 147–8
[52] Das S, Chen H Y, Penumatcha A V and Appenzeller J 2013 *Nano Lett.* **13** 100–5
[53] Perera M M, Lin M W, Chuang H J, Chamlagain B P, Wang C, Tan X, Cheng M M C, Tománek D and Zhou Z 2013 *ACS Nano* **7** 4449–58
[54] Chuang H J, Tan X, Ghimire N J, Perera M M, Chamlagain B, Cheng M M C, Yan J, Mandrus D, Tománek D and Zhou Z 2014 *Nano Lett.* **14** 3594–601
[55] Xu Y, He K T, Schmucker S W, Guo Z, Koepke J C, Wood J D, Lyding J W and Aluru N R 2011 *Nano Lett.* **11** 2735–42
[56] Tayran C, Zhu Z, Baldoni M, Selli D, Seifert G and Tománek D 2013 *Phys. Rev. Lett.* **110** 176805
[57] Vázquez de Parga A L, Calleja F, Borca B, Passeggi M C G, Hinarejos J J, Guinea F and Miranda R 2008 *Phys. Rev. Lett.* **100** 056807
[58] Selli D, Baburin I, Leoni S, Zhu Z, Tománek D and Seifert G 2013 *J. Phys.: Condens. Matter* **25** 435302
[59] Guan J, Zhu Z and Tománek D 2014 *Phys. Rev. Lett.* **113** 046804
[60] Bridgman P W 1914 *J. Am. Chem. Soc.* **36** 1344–63
[61] Tománek D 2014 *Mater. Express* **4** 545–7
[62] Narita S *et al* 1983 *Physica* B+C **117–8** 422–4
[63] Maruyama Y, Suzuki S, Kobayashi K and Tanuma S 1981 *Physica* B+C **105** 99–102
[64] Koenig S P, Doganov R A, Schmidt H, Castro Neto A H and Özyilmaz B 2014 *Appl. Phys. Lett.* **104** 103106
[65] Boulfelfel S E, Seifert G, Grin Y and Leoni S 2012 *Phys. Rev.* B **85** 014110
[66] Guan J, Zhu Z and Tománek D 2014 *ACS Nano* **8** 12763–8
[67] Guan J, Zhu Z and Tománek D 2014 *Phys. Rev. Lett.* **113** 226801
[68] Jamieson J C 1963 *Science* **139** 1291–2
[69] Boča R, Hajko P, Benco L, Benkovský I and Faktor D 1993 *Czech. J. Phys.* **43** 813–9
[70] Rivero P, Horvath C M, Zhu Z, Guan J, Tománek D and Barraza-Lopez S 2014 arXiv:1412.5944
[71] Zhu Z, Fthenakis Z G and Tománek D 2015 arXiv:1502.07050
[72] Qiu H *et al* 2013 *Nat. Commun.* **4** 2642
[73] Terrones H, Terrones M, Hernández E, Grobert N, Charlier J C and Ajayan P 2000 *Phys. Rev. Lett.* **84** 1716–9
[74] Tománek D 2014 *Guide Through the Nanocarbon Jungle: Buckyballs, Nanotubes, Graphene and Beyond* (Bristol, UK: IOP)
[75] Wei L, Kuo P K, Thomas R L, Anthony T R and Banholzer W F 1993 *Phys. Rev. Lett.* **70** 3764–7
[76] Anthony T R, Banholzer W F, Fleischer J F, Wei L, Kuo P K, Thomas R L and Pryor R W 1990 *Phys. Rev.* B **42** 1104–11
[77] Chen S, Wu Q, Mishra C, Kang J, Zhang H, Cho K, Cai W, Balandin A A and Ruoff R S 2012 *Nat. Mater.* **11** 203–7
[78] Zhao P, Einarsson E, Xiang R, Murakami Y, Chiashi S, Shiomi J and Maruyama S 2011 *Appl. Phys. Lett.* **99** 093104
[79] Fthenakis Z G and Tománek D 2012 *Phys. Rev.* B **86** 125418
[80] Fthenakis Z G, Zhu Z and Tománek D 2014 *Phys. Rev.* B **89** 125421
[81] Berber S, Kwon Y K and Tomanek D 2000 *Phys. Rev. Lett.* **84** 4613–6
[82] Balandin A A 2011 *Nat. Mater.* **10** 569–81